Materials for life sciences

In-vitro corrosion assessment of silicate-coated AZ31 Mg alloy in Earle's solution

M. Kalaiyarasan[1], K. Saranya[1], and N. Rajendran[1,*] (iD)

[1] *Department of Chemistry, College of Engineering Guindy, Anna University, Chennai, Tamil Nadu 600 025, India*

ABSTRACT

Magnesium alloys are promising materials for biodegradable implants. In the present investigation, AZ31 Mg alloy was anodized in alkaline silicate electrolyte and anodization time period was optimized. From the current transient ($i–t$) curve and corrosion analysis, it was confirmed that 60-min anodization was sufficient to obtain a silicate coating with a better corrosion resistance of 37.05 kΩ. The hydrophilic nature of the coating was confirmed by the contact angle measurement. XRD results revealed the formation of MgO (periclase) and biocompatible Mg_2SiO_4 (forsterite) phases. Hydrogen evolution studies showed that the degradation rate of the anodized sample correlated with the real-time corrosion behavior. At the end of 7 days of immersion in Earle's solution, bone-like apatite was precipitated with Ca/P ratio at 1.39 indicating the incorporation of silica in the apatite. From scanning electrochemical microscopic studies, the current density of anodized sample was found to be minimum and uniform over the entire surface. Increase in immersion time resulted in fluctuation in current density signifying the coating's interaction with Earle's solution and initiation of apatite formation.

Introduction

Magnesium (Mg) and its alloys are attractive candidates for multiple biomedical implanting applications such as cardiovascular stents and orthopedic implants [1]. It is suitable for load-bearing applications, because of its similar Young's modulus (41–45 GPa) and density (1.74–1.84 g/cm^2) which are closer to that of human bone, and it also offers better strength compared to biodegradable polymers [2, 3]. The usage of Mg as an implant is advantageous because it is biocompatible, non-toxic and the fourth most essential element present in the human body [4]. Bone is the major reservoir of Mg to the extent of approximately 50%. Mg acts as a co-factor for various essential enzymatic reactions in the synthesis of protein, plasma membrane and other cellular activities [5]. It degrades naturally within the body; hence, there is no need for revision surgery [6]. However, magnesium degrades faster compared to other metals due to its low corrosion resistance in a complex ion solution, mimicking the physiological environment, leading to dramatic hydrogen evolution and a rise in the pH [5, 7, 8]. As a result, the implant is unable to

Table 1 Brief summary of different surface modification technique and comparison of current density for Mg implant materials

S. No	Substrate	Process/electrolyte	Corrosion rate C_R mm/per year	Current density (i_{corr}) $\mu A/cm^2$	Medium	References
1	AZ91	Anodization process Na$_2$SiO$_3$ electrolyte	3.39	4.17	NaCl	[21]
2	AZ80	Micro-arc oxidation process Na$_2$SiO$_3$·H$_2$O + NaF + HA + K$_2$ TiF$_6$	–	0.056	SBF	[22]
3	AZ31B	Micro-arc oxidation process Na$_2$SiO$_3$	2.01×10^{-5}	0.05	Saline medium NaCl	[23]
4	AZ31B	Anodization process NaPO$_4$	1.61	35.31	HBBS	[24]
5	AZ31	Micro-arc oxidation Process NaF/Na$_2$SiO$_4$	–	0.29	NaCl	[25]
6	AZ91D	Anodization NaOH + Na$_2$SiO$_3$	41.2	27.0	0.15 NaCl	[15]
7	AZ31B	Anodization ZrO$_2$	–	2.796	SBF	[9]

provide sufficient time for the wound to heal completely. Moreover, the hydrogen generation decreases the survival rate of the organism and the pH rise causes tissue necrosis at the surgical site. In order to improve corrosion resistance and ensure clinical application [9], the surface is modified using various methods, viz. micro-arc oxidation [10], sol–gel [11], anodization [12], and conversion coating [13].

Among the several available methods, anodization is one of the effective surface treatments that forms thick and uniform oxide layer which can increase the corrosion resistance and bioactive nature [14]. The anodization is influenced by various parameters to ensure a uniform layer, i.e., voltage/current applied, choice of electrolytes, area of the electrodes, the distance between the electrodes, etc. [15]. Mizutani et al. [16] studied the formation of Mg(OH)$_2$ film using sodium hydroxide electrolyte at non-sparking anodization (3 V and 10 V) and sparking anodization (above 80 V) methods. The low-voltage anodization method is advantageous as it maintains the strength of the materials even after anodization [17]. So far, anodization is the most used method for ceramic oxide coating techniques [18]. The highly stable metal oxides, viz. ZrO$_2$, SiO$_2$, CeO$_2$, and MoO$_2$ are used effectively to enhance the corrosion resistance under the environmental conditions to protect Mg and its alloys [19]. Some researchers are interested in anodizing Mg in an alkaline electrolyte such as phosphate, silicate and borate solutions expecting the

formation of oxysalt to improve the corrosion resistance of AZ31 Mg alloy. Mg was anodized in the alkaline solution containing silicate and phosphate. The formed coating was found to protect protecting the surface effectively [20] One-step anodization of bioceramic compounds on Mg alloy to enhance surface properties and in vitro studies about the bioactivity to the coatings were explored [9] (Table 1).

Mechanical failure often occurs in Mg implants due to cracks, pitting and holes. Scanning electrochemical microscopy (SECM) is one of the most powerful techniques for localized corrosion research due to the broad diversity of operation modes which offer great flexibility to the technique. It is capable of identifying the active/passive region in a unique way by microscopic real-time investigation of the local changes in conductivity, physicochemical and biomedical studies of the corroding metal surfaces [26]. They are classified into three main modes, namely potentiometric, amperometric and alternating current (AC) modes. The amperometric and potentiometric modes are used to study the metal defects and pitting on the metal surface. SECM is widely used to study the corrosion behavior and electrochemical reactivity of metals, viz. iron, steel, aluminum, titanium, magnesium and its alloys [27–30]. To have a deeper understanding of the corrosion behavior of Mg, researchers have used potentiometric and amperometric modes to monitor the distribution of Mg^{2+} using redox mediator.

In the present investigation, the current density was monitored during the anodization process to optimize the anodization time. The anodized samples were evaluated before and after immersion to determine their ability to form apatite layer. To analyze the surface topography, functional groups and crystallographic structure, techniques like attenuated total reflectance-Fourier transform infrared spectroscopy (ATR-FTIR), X-ray diffraction (XRD), and scanning electron microscopy (SEM and EDAX) were employed. The overall and localized corrosion resistance behavior were evaluated by potentiodynamic polarization, electrochemical impedance spectroscopic (EIS) and scanning electrochemical microscopic (SECM) techniques.

Materials and methods

Sample preparation

AZ31 Magnesium alloy was procured from Seoul National University, South Korea. AZ31 Mg alloys with the mass fraction of Al 3%, Zn 1%, Mn 0.2% and balance Mg were used for investigation. The sample dimension chosen was 15 mm × 15 mm × 2 mm. The samples were polished with 1000–2000 grades silicon carbide (SiC) abrasive paper. Then, the samples were thoroughly cleaned by ultrasonication with acetone followed by distilled water.

Electrochemical anodization of AZ31 Mg alloy

The chosen AZ31 Mg alloy was anodized in a solution containing sodium silicate and sodium hydroxide (0.2 M Na_2SiO_3 + 0.1 M NaOH) as the electrolyte. This experiment was carried out with two-electrode system: the test sample as anode and platinum as the cathode. The electrodes were kept at a distance of 1.5 cm in the electrolytic solution. A direct current (DC) power source (M/s Alpha Model L1285) was used, and a potential difference of 10 V was applied for different time periods, viz. 10, 20, 40, 60 and 80 min. The anodized sample was washed with distilled water and dried at room temperature. It was kept in desiccator to prevent any possible reaction with atmospheric air and moisture.

Surface characterizations

The surface morphology and elemental composition of the 60-min anodized samples were analyzed using field-emission scanning electron microscopy (FESEM, JEOL-JSM 7600F) equipped with energy-dispersive X-rays analysis (EDX-Oxford instruments). The functional groups present in the 60-min anodized sample were analyzed with attenuated total reflectance-Fourier transform infrared spectrometer (ATR-FTIR, Jasco FT/IR Model 4700) in the wave number range 4000–500 cm^{-1}. The phase crystalline composition of the sample was studied by Xpert Pan Pro Analytical X-ray diffractometer (XRD) using Cu Kα radiation in the range of 20°–80° at a scan rate of 1°/s, and the surface wettability of the samples was measured using a contact angle analyzer (model Phoenix 300 Plus) with a drop volume of 8 μl.

Immersion studies

Earle's solution was prepared by dissolving the following chemicals: sodium chloride 6.8 g, potassium chloride 0.4 g, calcium chloride 0.2 g, magnesium sulfate 0.1 g, sodium phosphate monobasic hydrate 0.14 g, sodium hydrogen carbonate 2.2 g, D-glucose 1.0 g in 1000 ml deionized water. Finally, the pH was adjusted to 7.4 using 1 M HCl [31, 32]. The anodized AZ31 Mg alloy was immersed for 7 days at room temperature in freshly prepared Earle's solution, to evaluate the bioactivity of samples. The immersed samples were further analyzed by SEM & EDAX, XRD, ATR-IR and electrochemical studies.

Hydrogen evolution studies: the sample was hung in the middle of the beaker with thread. An inverted burette with funnel setup filled with Earle's solution was kept over it. The volume of hydrogen evolved and the rate of corrosion was measured for 7 days.

Electrochemical studies

Electrochemical corrosion behavior of uncoated, anodized and immersion samples was tested in Earle's solution at room temperature. The experiments were carried out using Autolab (PGSTAT 302 N, Metrohm B.V., Netherlands) in a conventional three-electrode system; platinum foil as the counter electrode, saturated calomel electrode (SCE) as reference electrode and test specimen as working electrode with 1 cm^2 exposed surface area. The samples were

subjected to open-circuit potential (OCP) measurement for 30 min to get a steady-state potential. Electrochemical impedance studies were performed in the frequency range of 0.01 Hz to 100 kHz with an applied sinusoidal potential of ± 10 mV. To investigate the corrosion behavior, potentiodynamic polarization studies were done in the potential range − 2.0 to 0.5 V at a scan rate of 1 mV s^{-1} with an exposed area of 1 cm^2 in Earle's solution. From the polarization resistance (R_p), corrosion potential (E_{corr}) and corrosion current density (i_{corr}) values, the corrosion rate is calculated using Stern–Geary Eq. (1),

$$R_p = \beta_a x \beta_c / 2.3 i_{corr}(\beta_a + \beta_c) \tag{1}$$

where β_a and β_c are the slopes of anodic and cathodic polarizations, i_{corr} is corrosion density, and R_p is the polarization resistance [33, 34].

Scanning electrochemical microscopic studies

The uncoated and anodized samples were analyzed using scanning electrochemical microscope (SECM, Uniscan Model M470 with the software version 1.43). All the experiments were carried out with three-electrode system, in which the platinum foil was used as the counter electrode, saturated calomel electrode as the reference electrode and test sample as the working electrode. An ultra-microelectrode (UME) 15 µm sensing probe was used to investigate the sample. All the experiments were carried out in Earle's solution at room temperature. The probe tip was scanned at a constant potential and capable of moving in x, y and z directions of the sample. The distance between the probe and sample was kept at 10 µm and was adjusted with the help of a video camera system [26, 35]. The schematic setup is shown in Fig. 1.

Anti-biofilm assay

The biofilm estimation was done using *Pseudomonas aeruginosa* (gram negative) and *Staphylococcus epidermis* (gram positive), which were grown in Luria Broth (LB) and Tryptone Soya Broth (TSP) medium, respectively. The absorbance of bacterial culture was adjusted to 0.5 at optical density (OD$_{570nm}$). 20 µl of cell suspension and 180 µl of the media were added to 96-well microplate. The plates were incubated at 37 °C for 4 h, and each well was washed thoroughly
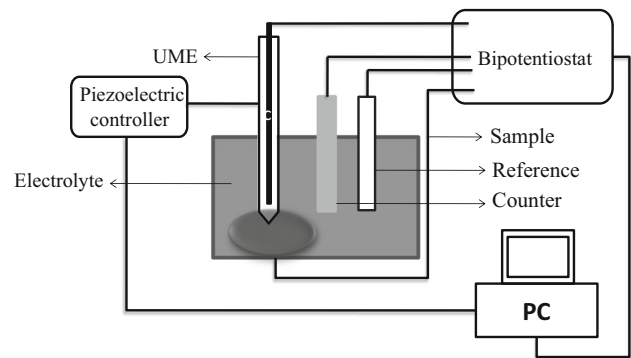

Figure 1 The schematic representation of SECM experimental set up.

with phosphate buffer saline (PBS) to remove the planktonic and killed cells. The adhered cells were stained with 0.2% (w/v) crystal violet solution for 5 min and dried. The adhered crystal violet cells were dissolved in 95% ethanol, and OD was measured at 570 nm using a microplate reader (Multiskan, Thermo Labsystem, and Beverly, MA, USA.)

Results and discussion

Electrochemical anodization and SEM analysis

Figure 2 shows the current transient (*i–t*) curve of anodized AZ31 Mg alloy in alkaline silicate electrolyte, with a constant applied potential of 10 V. In the initial stage of anodization, there was a gradual increase in current due to Mg dissolution into the solution and the formation of a barrier layer on the substrate [36]. After which, there was a gradual
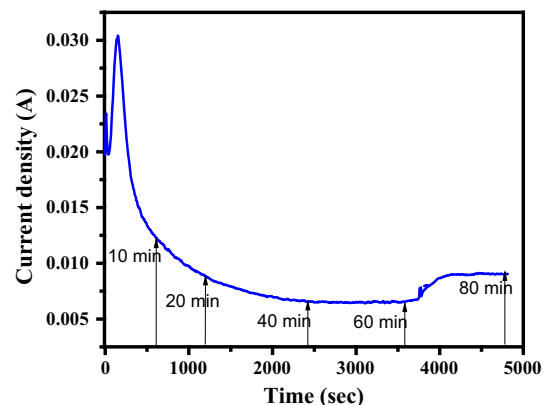
Figure 2 Current transient (*i–t*) curve for anodization of AZ31 Mg alloy.

decrease in the current till 20 min. Under the influence of the electric field, Mg^{2+} ions dissolute from the metal surface along with the evolution of O_2 due to the decomposition of OH^- ions. The effect of potential difference leads to the migration of OH^- and SiO_3^{2-} ions toward the anode. The migrated ions led to the formation of interfacial film between the electrolyte and electrode.

The SEM images showed the morphology of the anodic coatings at different time periods in silicate electrolyte and are shown in Fig. 3. The samples anodized for 10 and 20 min exhibited the current density of 120 and 8.7 mA, respectively. The deposition of the anodic layer with micro- and nano-agglomerate structure is shown in Fig. 3a, b. Even after 40 min of anodization, the surface was not uniform and the current density was around 6.7 mA and is shown in Fig. 3c. The continual decrease in current density indicated the formation of progressing the anodic layer. The current density was stabilized at 6.5 mA after 60 min of anodization indicating the attainment of steady state during which a uniform thick layer of silicate and oxide was formed and is represented in Fig. 3d [37]. As the anodizing time was extended to 80 min, the sudden increase in current density of 9.1 mA was observed due to peeling of the anodic surface. From the current transient curve and SEM analysis, 60-min anodization in silicate electrolyte was found to be sufficient to form a uniform anodic layer. Hence, all other experiments were conducted with the 60-min anodized sample.

The surface morphology, elemental mapping and cross section of the anodized sample are shown in Fig. 4. The morphology of sample anodized for 60 min showed non-uniform and rough surface film formation with less protuberance structure due to the evolution of oxygen during the anodization process [38]. The elemental composition was detected by EDX analysis and is displayed in Fig. 4b. The presence of Mg, Si and O was observed from the EDX profile, the ions were distributed in the entire surface, and the distribution was confirmed by EDX mapping.

The bioactivity of the anodized sample was evaluated in Earle's solution for an initial period of 7 days, and the results are shown in Fig. 5. The surface showed the formation of cracks and nanospherical agglomerate structure. The existence of cracks may be attributed to the effect of dehydration and shrinkage of the coating surface along with the formation of an apatite layer. The average coating thickness after immersion was measured to be 9.8 μm, which was higher than the value obtained before immersion and is shown in Fig. 5b. EDX mapping revealed even distribution of calcium, phosphate and oxygen along with the silica coating. The EDX profile confirmed the elemental composition of apatite particles as shown in Fig. 5c. The Ca/P ratio was found to be 1.39 which was less than the
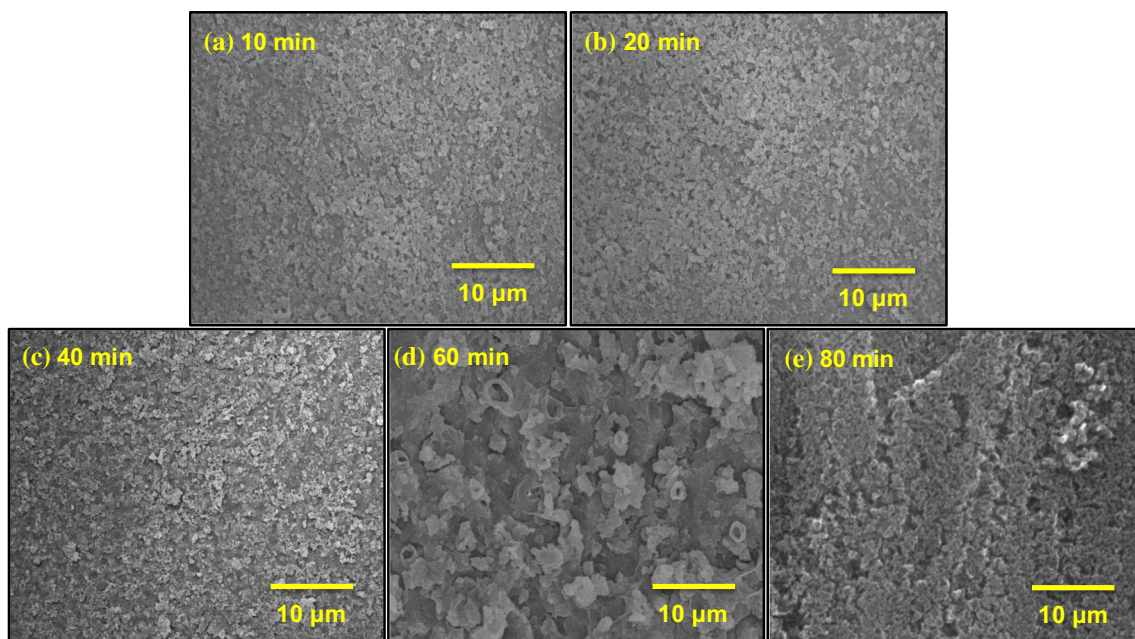
Figure 3 SEM images of anodized samples at various time periods.
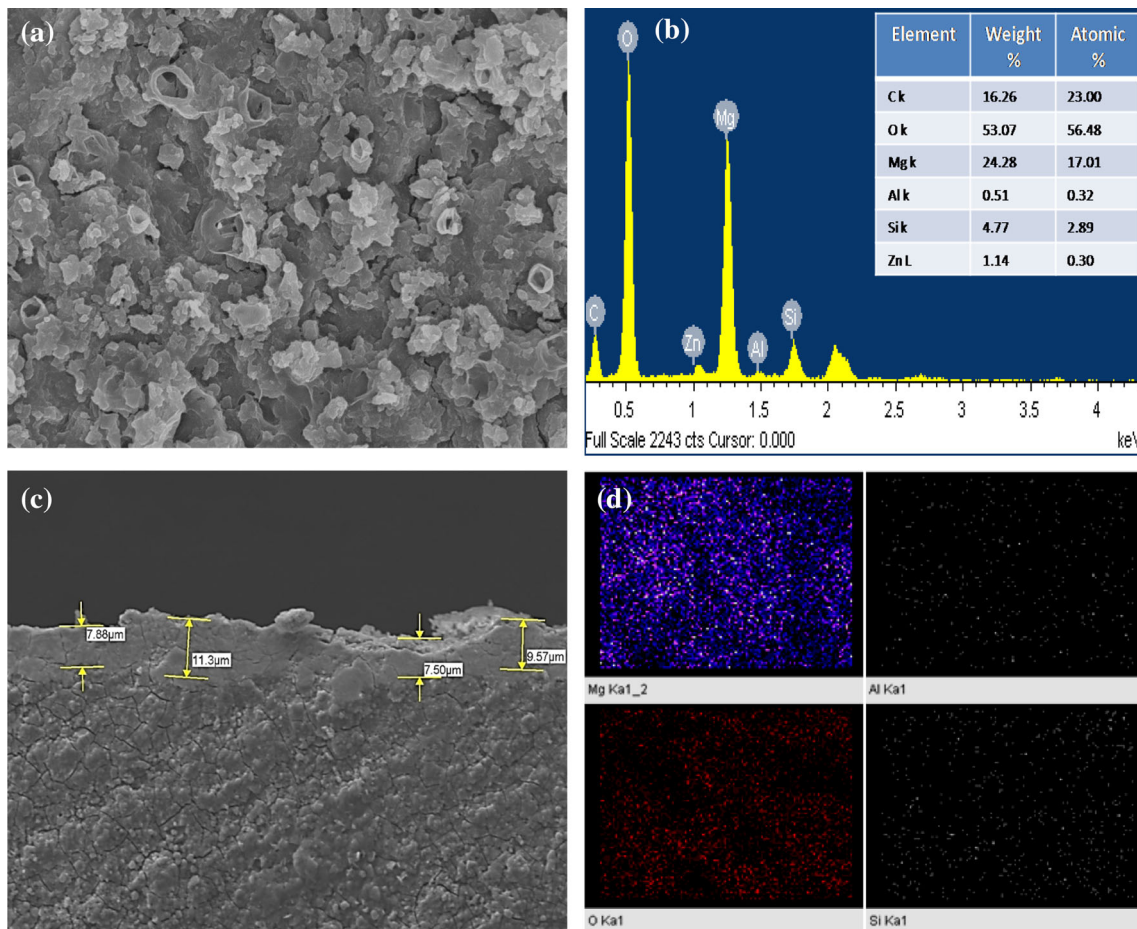
Figure 4 The anodized sample **a** SEM image, **b** EDX profile, **c** cross section and **d** EDX mapping.

value of biological apatite. The reason for the lesser value could be ascribed to the substitution of some of the Ca^+ ions by the Mg^{2+} ions, and the magnesium incorporated apatite is considered significant in the bone formation [39].

ATR-FTIR and XRD studies

The ATR-FTIR spectra of the anodized and immersion sample are shown in Fig. 6. The anodized sample (Fig. 6a) showed sharp and broad peaks at 3670 and 3640–2900 cm^{-1} which were assigned to -OH groups. Bending vibration of H–O–H bond peak was observed at 1609 cm^{-1} [39]. The presence of a strong band at 1027 cm^{-1} was attributed to Si-O-Si asymmetric stretching mode [40]. The peak for the vibrational mode of metal oxide was seen at 500 cm^{-1} due to the formed coating, which was composed of Mg$_2$SiO$_4$ and MgO [41].

The ATR-FTIR spectrum of the anodized sample immersed in Earle's solution for 7 days is shown in

Fig. 6b. The bands observed at 1016, 845 and 551 cm^{-1} were due to asymmetric bending of PO_4^{3-} and the formation of Si-HAp, respectively [42]. The overlapping phosphate and Si–O–Si groups were identified at the band of 1016 cm^{-1}. The peak obtained at 1424 cm^{-1} was due to the carbonate [43], which was formed as a result of OH$^-$ reacting with carbon dioxide in the atmospheric air. The broadband observed between 3750 and 3000 cm^{-1} was attributed to –OH group [8]. From the peaks observed, apatite formation was confirmed on the anodized sample surface after 7 days of immersion.

The anodized sample was analyzed using XRD before and after exposure in Earle's solution, and the results are shown in Fig. 7. The peaks at 34.9° and 69.3° correspond to the base metal Mg and the peaks at 2θ values 36.9°, 43.0°, 63.7°, and 78.7° signified the formation of MgO. The characteristic peaks at 2θ values of 32.7°, 36.9°, 38.1° and 58.1° belonged to Mg$_2$SiO$_4$. These findings confirmed that the coating
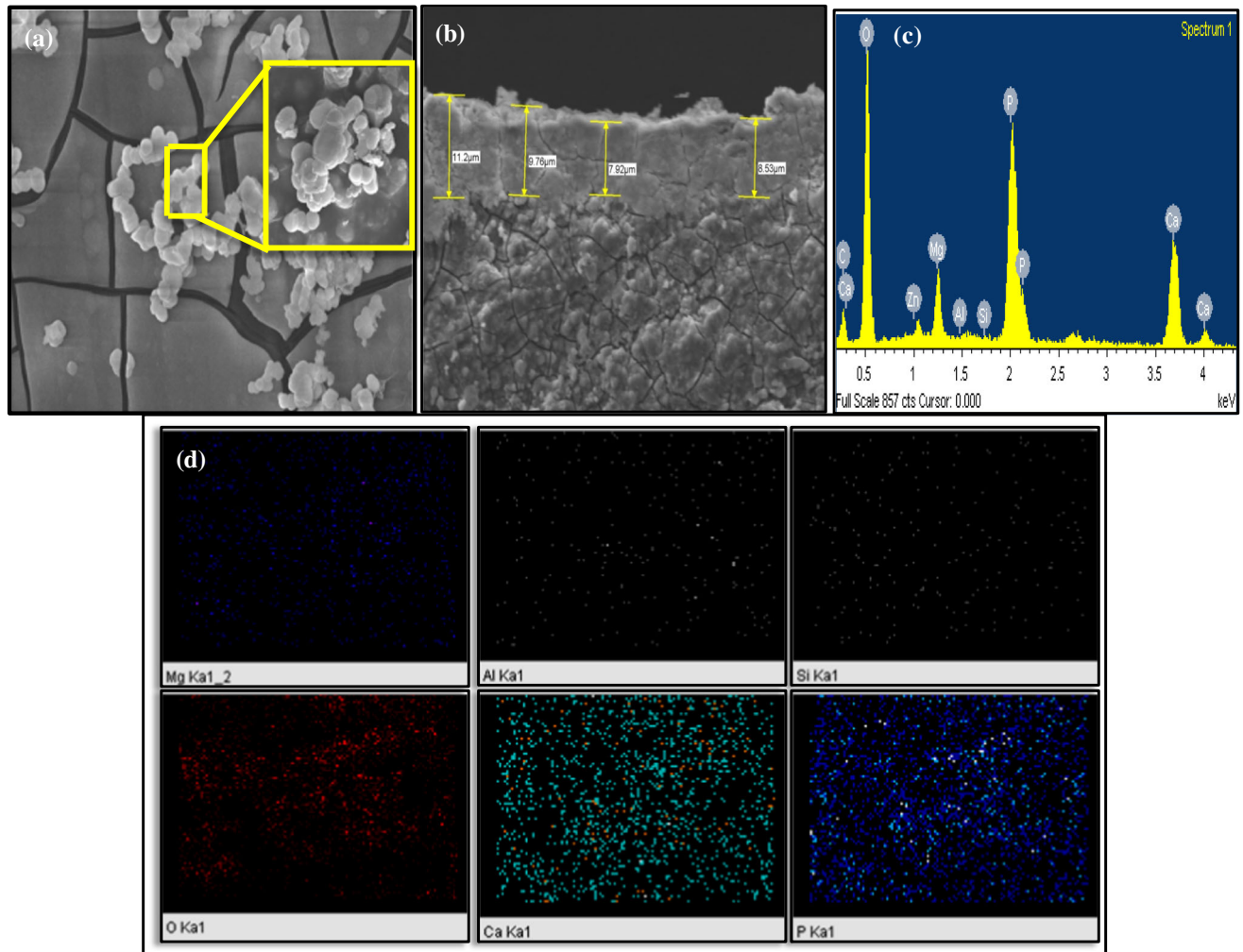
Figure 5 SEM images of silicate anodized Mg alloy immersed in Earle's solution for 7 days; **a** morphology, **b** cross section, **c** EDX profile and **d** EDX mapping.

consisted of MgO (periclase) and biocompatible Mg_2SiO_4 (forsterite) [44–47]. The obtained coating was pure and crystalline in nature.
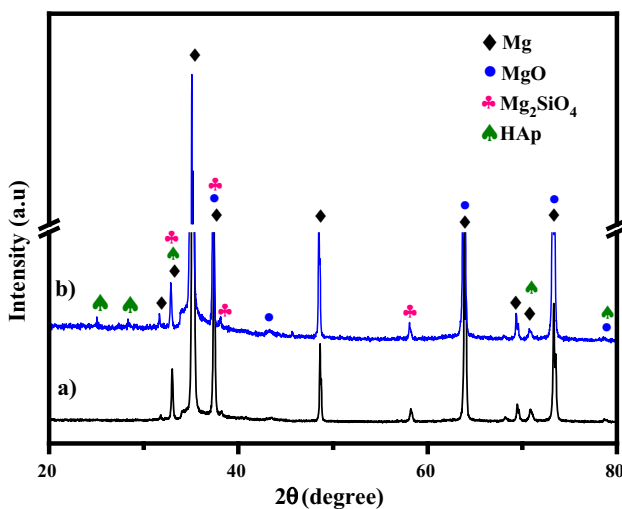
The exposure of the anodized sample in Earle's solution caused the dissolution of the coating. Mg_2SiO_4 present in the coating gets converted to Mg^{2+} and silicate ion, which reacted with the physiological-like solution and formed silicic acid which led to the deposition of Ca^{2+} and PO_4^{3-} ions. The new crystalline peaks with less intensity at 25.1°, 28.3° and 70.8° confirmed the HAp formation as shown in Fig. 7b [48]. The other peaks of HAp coincided with substrate peaks. Hence, it is evident that the anodized sample showed bioactivity and induced bone formation [49, 50].

Contact angle measurements

The contact angle measurement helps to determine the hydrophilic or hydrophobic nature of the surface. The surface wettability plays a major role in ensuring cell adhesion and proliferation. The surface wettability of the uncoated, anodized sample before and after immersion in Earle's solution for 7 days was studied. The water contact angles (Fig. 8) of uncoated, anodized sample and immersion samples were 77 ± 2.1°, 35 ± 1.3° and 22 ± 3°, respectively. The coated sample showed hydrophilic nature (i.e., the contact angle decreased) due to the interaction of hydroxyl group in silanol and water molecules [51]. The immersion sample showed a lower contact angle when compared to anodized and uncoated sample. After 7 days of immersion, the chemical constituents
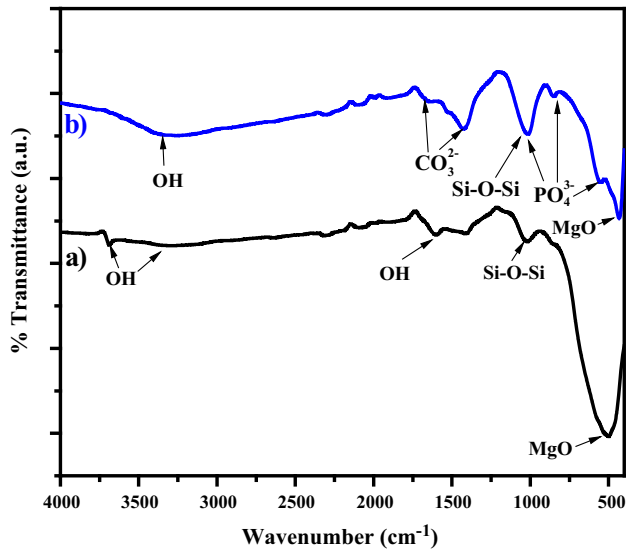
Figure 6 ATR-FTIR spectra of anodized sample **a** before and **b** after immersion in 7 days in Earle's solution.

Figure 7 XRD spectra of anodized sample **a** before and **b** after immersion in Earle's solution for 7 days.

of the coating had remarkably changed leading to a further decrease in contact angle [8, 49]. The hydrophilic nature of the coating favors cell adhesion and proliferation. Spriano et al. [52] have reported that the contact angle below 29° is most suitable for cell proliferation and osseointegration.

Hydrogen evolution

The rate of hydrogen evolution of the uncoated and anodized sample was investigated by immersing them in Earle's solution for 7 days, and the results are
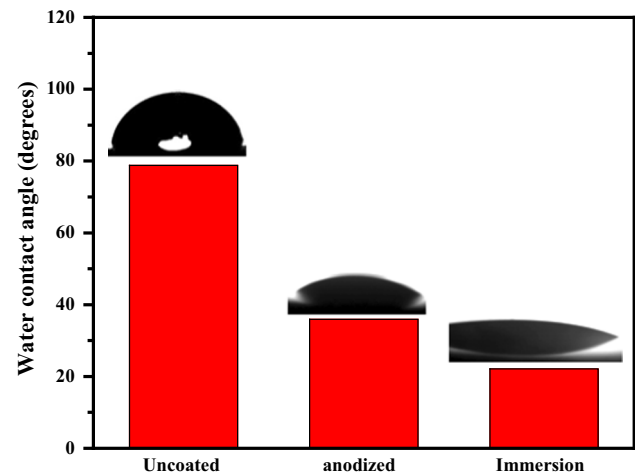

Figure 8 Water contact angle measurements of uncoated, anodized and immersion samples.

shown in Fig. 9a. In the uncoated sample, the ions of the physiological-like solution initially reacted with the Mg surface and H_2 gas was evolved. The rate of hydrogen evolution helped in estimating the real-time corrosion taking place in Mg. The evolution of hydrogen gas was around 2.05 mL/cm^2 and 5.9 mL/cm^2 after 24 h and 168 h, respectively. The rate of hydrogen evolution varied each day. This could be attributed to the formation and dissolution of the oxide layer. The hydrogen evolution was very high due to the loosely bound oxide layer which was formed at a pH of around 7.4 [53]. The attack of chloride ions on the loosely bound layer caused the dissolution of the layer at a faster rate. As time progressed, the formed $Mg(OH)_2$ layer was stabilized due to the increase in pH and the hydrogen evolution was reduced. The hydrogen evolution for the anodized sample was at 0.3 and 1.8 mL/cm^2 after 24 and 168 h, respectively. The hydrogen evolution rate was greatly reduced due to the passive silicate film.

The corrosion rate was calculated using the volume of hydrogen generated by the sample and is shown in Fig. 9b. The corrosion rate of the uncoated sample was 4.51 and 0.91 mm/year after 24 and 168 h, respectively, whereas the corrosion rate of the anodized sample was 0.04 mm/year and 0.72 mm/year, respectively, for the same duration. The degradation rate was significantly low showing that the anodized sample minimized the penetration of aggressive ions into the substrate. In addition, the corrosion rate of immersion sample obtained from hydrogen evolution
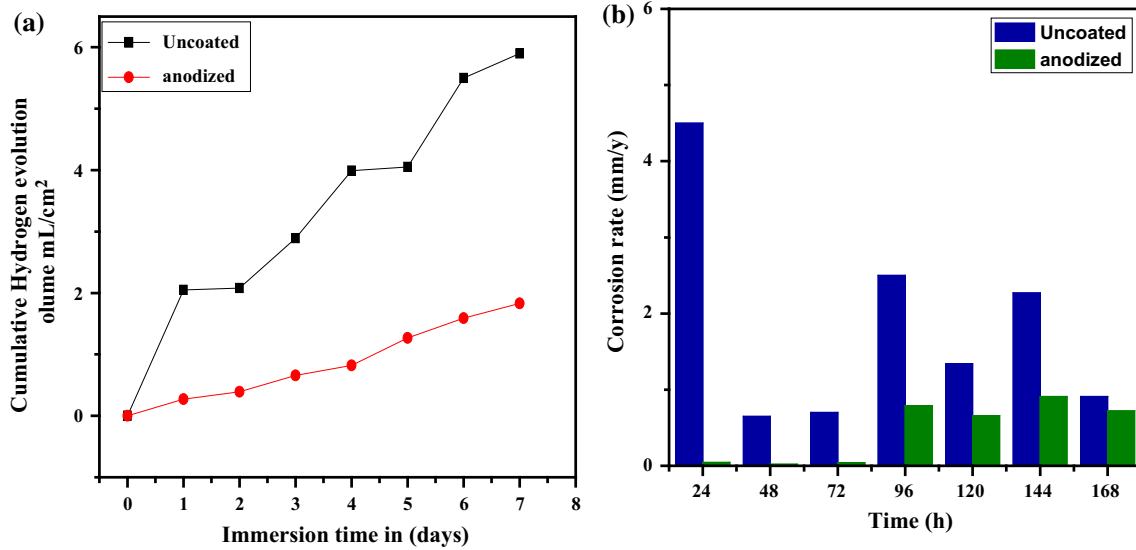
Figure 9 **a** Hydrogen evolution and **b** corrosion rate of uncoated and anodized sample was calculated from the evolved hydrogen volume.

studies was almost similar to the corrosion rate obtained from potentiodynamic polarization data.
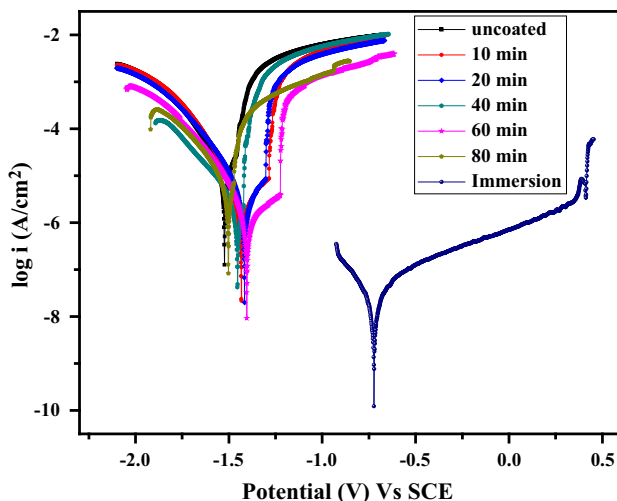
Electrochemical studies

Potentiodynamic polarization

Potentiodynamic polarization curves of the uncoated, anodized and immersion samples in Earle's solution are shown in Fig. 10, and the parameters obtained from the polarization curves are given in Table 2. The (i_{corr}) values were found to be 14.45, 1.16, 4.40, 2.95, 0.18 and 17.85 $\mu A/cm^2$ for the uncoated and

Figure 10 Potentiodynamic polarization plots of uncoated, anodized sample and immersion sample in Earle's solution.

anodized samples at 10, 20, 40, 60 and 80 min duration, respectively. The corrosion potentials of the anodized samples were shifted toward the nobler direction, to a maximum extent of 120 mV compared to the uncoated. This showed that the anodic film formed with Mg-Si-O complex on the surface could effectively reduce the corrosion rate and protect the metal surface [45]. Among the samples anodized at different time periods, 60-min anodized sample showed better corrosion resistance. It was observed from the anodic region of the curves, 60-min anodized sample could withstand up to the potential of -1.25 V after which breakdown of the passive film occurred. The observed homogeneity on the 60-min anodized sample surface was responsible for similar corrosion resistance which matches the previous reports. Xue et al. [23] have used micro-arc oxidation method to deposit the coating with a current density of 0.05 $\mu A/cm^{-2}$, whereas the result obtained in our work was almost on par with them using a low potential of 10 V itself and a current density of 0.18 $\mu A/cm^{-2}$. On the whole corrosion rate (C_R) and the polarization resistance (R_p) of 60-min anodized sample were better than the uncoated and other samples. Hence, further investigations were done with the 60-min anodized sample.

The anodized sample was immersed in Earle's solution for 7 days, and it showed a significant shift toward the positive direction in the E_{corr} (680 mV) in contrast to uncoated and other anodized samples. The immersion sample exhibited reduced (i_{corr}) of

Table 2 Potentiodynamic polarization behavior in Earle's solution at room temperature

Sample name	E_{corr} (V)	i_{corr} ($\mu A/cm^2$)	Break down potential (V)	Corrosion rate, C_R $\times 10^{-3}$ (mm/year)	Polarization resistance R_p (kΩ)
Uncoated	− 1.52	14.45	− 1.45	330	2.61
10 min	− 1.43	1.16	− 1.28	26	16.02
20 min	− 1.41	4.40	− 1.30	100	11.86
40 min	− 1.45	2.95	− 1.46	76.9	14.85
60 min	− 1.40	0.18	− 1.22	4.27	37.05
80 min	− 1.50	17.85	− 1.40	417	4.88
Immersion	− 0.72	0.03	0.39	0.91	169.50

0.03 $\mu A/cm^2$ due to the growth of apatite layer on the anodized sample. [43]. The formed apatite layer coating was stable over a wide range of potential, and break down occurred at 0.39 V. The corrosion rate was decreased by several folds for the immersed anodized sample.

## Electrochemical impedance spectroscopic studies

Electrochemical impedance spectroscopy (EIS) studies of uncoated, anodized and immersion samples were conducted in Earle's solution and are illustrated in Fig. 11. The Nyquist plot of the uncoated sample revealed that the first capacitive loop in the high-frequency region was due to the charge transfer resistance between the metal oxide and Earle's solution. The second capacitive loop in the mid-frequency region occurred due to the resistance offered toward

the mass transportation of $Mg(OH)_2$, and the inductive loop seen in the low-frequency was due to the penetration of aggressive ions from Earle's solution [54].

The anodized sample exhibited a capacitive loop in the high-frequency region that could be attributed to charge transfer resistance of double layer, formed between coating and Earle's solution. A second capacitive loop occurred in the mid-frequency due to the relaxation of mass transport in solid phase, i.e., to growth of the corrosion product layer. The inductive loop occurred in the low-frequency region could be attributed to the penetration of corrosive ions on the substrate [55]. The immersion sample exhibited two capacitive loops; the first capacitive loop was due to the charge transfer reaction between the double layer which was formed on the silicate incorporated apatite layer and Earle's solution. The second capacitive loop was due to the resistance offered at the interface of the coating/substrate.

From the Nyquist plot, it was seen that as the anodization time increased, the diameter of the capacitive loop also increased and the inductive loop decreased till 60 min. Among the samples, 60-min anodized sample exhibited better corrosion resistance due to the hindrance of aggressive ions penetration from Earle's solution through the anodic coating. After 7 days of immersion, the 60-min anodized sample showed only two capacitive loops and the inductive loop vanished completely indicating the improved corrosion resistance due to the apatite formation.

The EIS data were analyzed with an appropriate equivalent circuit using Zsimpwin software 3.21 and fitted with low Chi-square value of 10^{-4} to 10^{-3} and are shown in Fig. 12. For the substrate, R_S, R_1 and R_2 represent the solution resistance, oxide film
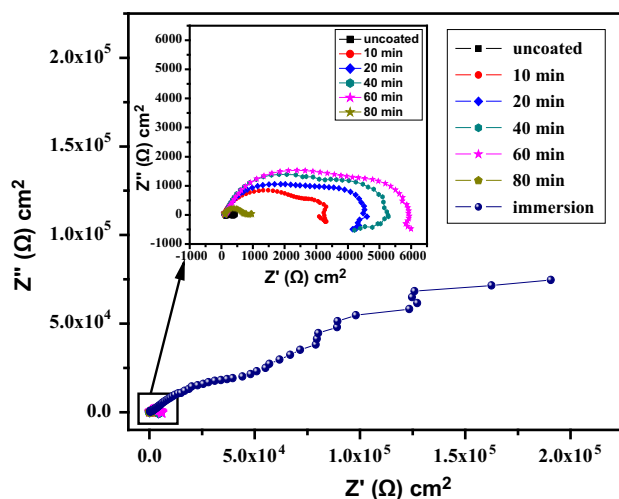
Figure 11 Nyquist plots of uncoated, anodized and immersion sample in Earle's solution.
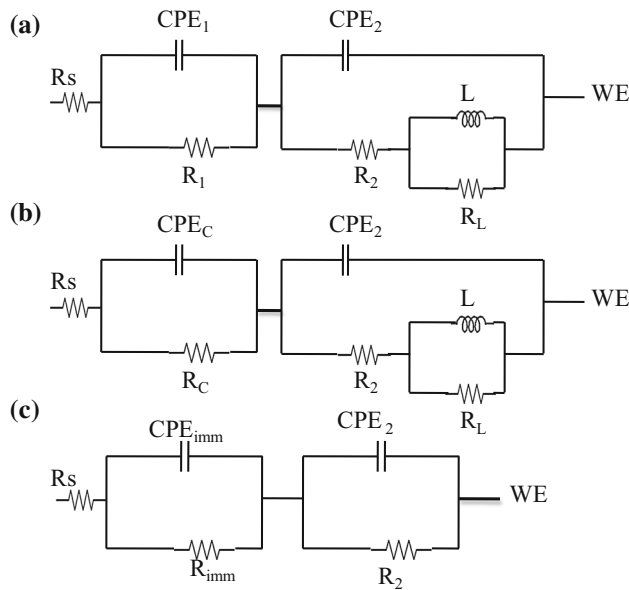
Figure 12 Equivalent circuit of **a** uncoated, **b** anodized, and **c** immersion sample.

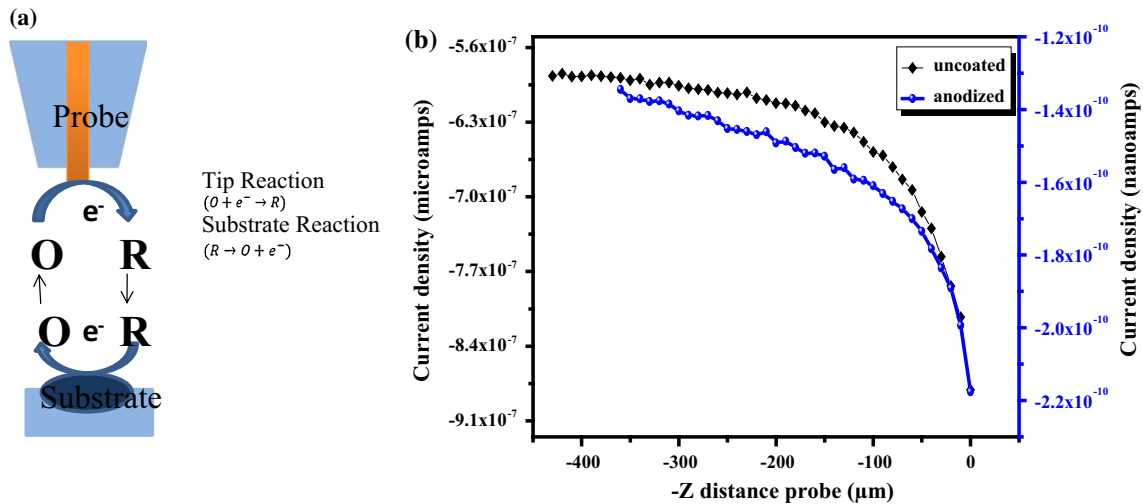the apatite coating. The obtained parameters from equivalent circuits are given in Table 3.

From the EIS data, it was observed that the anodized sample exhibited better corrosion resistance than the uncoated. In the anodized sample, the resistance of the coating (0.81 $K\Omega$ cm^2) was lesser than the interfacial resistance (5.96 $K\Omega$ cm^2) as a result of the porous structure. However, the pores were closed (observed from SEM) which prevented the entry of the ions into the substrate, thereby increasing the corrosion resistance. After 7 days of immersion in Earle's solution, R_{imm} was considerably increased. The resistance of R_2 was higher than R_{imm} indicating that the formed coating was still interacting with Earle's solution. Nevertheless, the substrate was well protected and the corrosion rate was diminished.

Scanning electrochemical microscopic studies

The samples were analyzed using the amperometric mode of scanning electrochemical microscopic (SECM) sample generation/tip collection (SG/TC) and are schematically shown in Fig. 13a. In the UME probe, only one reaction takes place, i.e., $(O + e^- \rightarrow R)$, where O (oxidant) is reduced to R (Reductant) and the R is oxidized back to O [56]. The approach curve experiment was done in the feedback mode; the tip will move in the $-Z$ direction toward the sample surface starting from a distance of 500 μm. Subsequently, the distance between the sample surface and tip was maintained below 30 μm,

resistance and charge transfer resistance, respectively. CPE_1 and CPE_2 are the constant phase elements of the oxide film and the double layer of the substrate, respectively. R_L and L are the inductive resistance and inductance of the substrate, respectively. In the anodized sample, R_C and CPE_C correspond to coating resistance and the constant phase elements of the coating. R_{LC} and L_C are the inductive resistance and inductance of the coating, respectively. R_{imm} represents the formed apatite coating resistance and CPE_{imm} denotes the constant phase element of

Table 3 EIS data obtained using Zsimp software for uncoated, anodized and immersion sample

Parameter	Uncoated	60 min anodized sample	Immersion
CPE_1 μS s^n cm^{-2}	2.33	–	–
n_1	0.63	–	–
R_1 kΩ cm^2	0.10	–	–
CPE_c μS s^n cm^{-2}	–	2.67	–
n_c	–	0.66	–
R_c kΩ cm^2	–	0.81	–
CPE_{imm} μS s^n cm^{-2}	–	–	0.12
n_{imm}	–	–	0.81
R_{imm} kΩ cm^2	–	–	14.6
CPE_2 μS s^n cm^{-2}	7.05	2.37	2.21
n_2	0.91	0.65	0.47
R_2 kΩ cm^2	0.14	5.96	106.1
L H	3.52	0.01	–
R_L kΩ cm^2	0.23	0.63	–

(a)

Probe

Tip Reaction
$(O + e^- \rightarrow R)$
Substrate Reaction
$(R \rightarrow O + e^-)$

O **R**

O **R**

Substrate

(b)

Figure 13 **a** The schematic representation of redox process taking place between UME and substrate of probe, **b** approach curves of uncoated and anodized sample in Earle's solution.
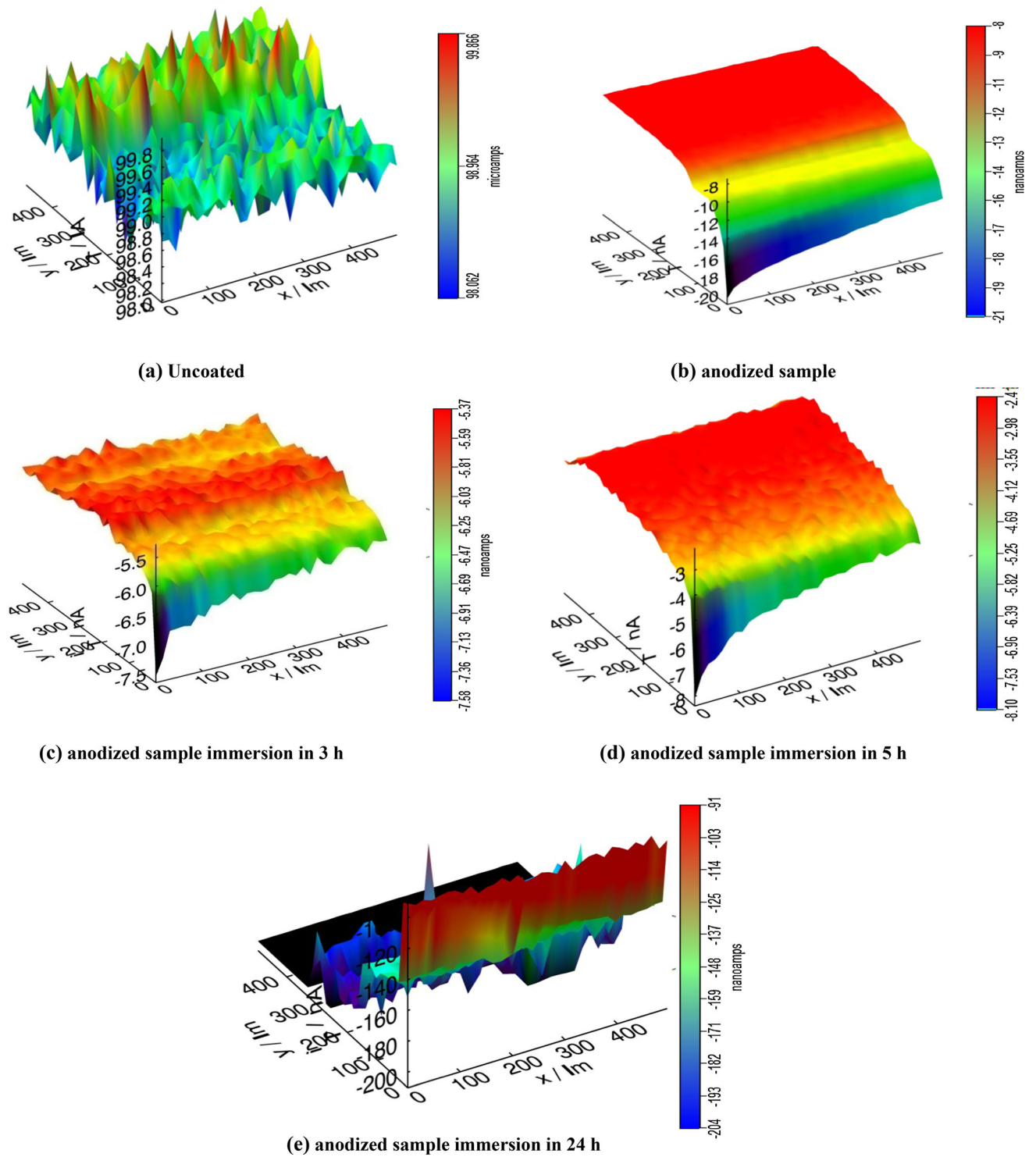
in order to monitor the current effectively. The tip and sample were applied with the corrosion potential E_{corr} and breakdown potential, respectively, for all the samples. The data obtained in the SECM analysis are in correlation with the potentiodynamic polarization studies and are shown in Fig. 13b.

The 3D images of localized corrosion current density monitored for the uncoated and anodized sample, exposed in Earle's solution, are given in Fig. 14. The image clearly shows that the uncoated sample exhibited a maximum corrosion current density of 99 $\mu A/cm^2$. Non-uniform current density was observed due to polarization of the uncoated sample, and H_2 gas was evolved due to the formation of localized pitting corrosion, resulting in uneven corrosion of the uncoated sample surface [57]. The anodized sample exhibited wavy nature on the surface and is shown in Fig. 14b. It produced the maximum current density of -8 nA/cm^2. The lower current density on the anodized sample indicated that the coating was cathodically protective and corrosion hardly occurred. The homogenous distribution of current density on the surface showed that pitting did not take place. The anodized sample was immersed in Earle's solution for 3, 5 and 24 h, and the results are shown in Fig. 14c–e. The 3- and 5-h immersion samples revealed that the coating was still cathodic protective, and the current density was slightly increased from -5.5 to -3 nA/cm^2. It could be attributed to the interaction of the coating with

Earle's solution. However, the coating was intact and protective. After 24 h of immersion, the ups and downs in the current density of the coating (-204 to -91 nA/cm^2) indicated non-uniformity of the surface due to the formation of apatite layer which could offer more cathodic protection for the Mg substrate [58, 59]. The SECM mapping showed that the coating was protecting the surface and deposition of HAp could have been initiated after 24 h of immersion. The pitting on the surface was greatly reduced in the anodized sample, and it exhibited better corrosion resistance than the uncoated sample. The varying current density of an anodized sample at different immersion time periods indicated that the coating interacted with the surface and led to the deposition of apatite. This is the ultimate goal in the orthopedic application.
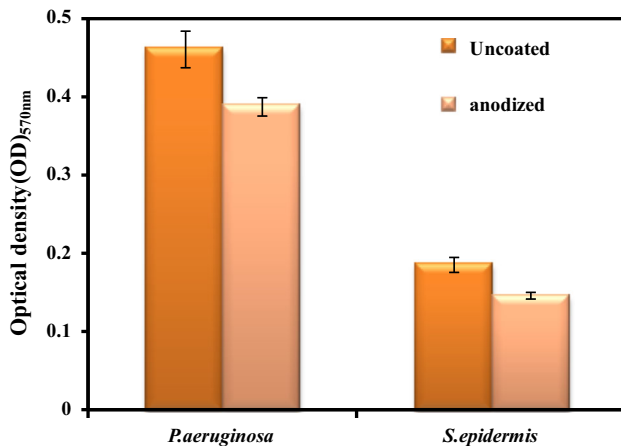
Anti-biofilm assay

The uncoated and anodized samples were incubated with *P. aeruginosa* and *S. epidermis* for 4 h to evaluate the anti-biofilm formation, which is shown in Fig. 15. The bacterial biofilm formation on the uncoated sample was considered as 100%. In the gram-negative bacteria (*P. aeruginosa*), the anodized sample exhibited a reduced rate of 15% in biofilm formation. The gram-positive bacteria (*S. epidermis*) showed 20% decrease in the biofilm formation. The presence of silica group in the coating was responsible for the

(a) Uncoated

(b) anodized sample

(c) anodized sample immersion in 3 h

(d) anodized sample immersion in 5 h

(e) anodized sample immersion in 24 h

Figure 14 3D- images from SECM mapping **a** uncoated, **b** anodized sample, **c** 3 h immersion, **d** 5 h immersion, **e** 24 h immersion samples in Earle's solution.

anti-biofilm activity. The interaction between the bacterial cell wall and hydrogen bond of silica group destabilized the peptidoglycan layer and leaked its content causing cell death. The toxicity of silicic acid in mammalian cells could be greatly reduced due to the electrostatic repulsion between the cell and silanol group [60].

Figure 15 Anti-biofilm formation assay.

Conclusion

1. In the present work, AZ31 magnesium alloy samples were anodized with silicate electrolyte at 10 V for different time periods. From the potentiodynamic polarization studies, the 60-min anodized sample was optimized for better corrosion resistance performance. Further investigations were done with 60-min anodized sample.

2. The morphological surface characterization showed rough surface with less protuberance structure of the sample. The phase crystalline composition revealed the formation of MgO (periclase) and biocompatible Mg_2SiO_4 (forsterite). The contact angle measurement exhibited hydrophilic nature which supported cell attachment.

3. After 7 days of immersion in Earle's solution, the SEM images clearly showed the nanospherical agglomerate structure on the coated surface consists of Ca and P. The apatite composition with less than 1.6 Ca/P ratio induced the bone formation. The potentiodynamic polarization studies showed significant increase in E_{corr} value toward the nobler positive direction.

4. Localized corrosion was monitored by SECM analysis. In anodized sample, the cathodic protective behavior of the coating was observed. After 24-h immersion in Earle's solution, the surface became more and more cathodically protective due to the incorporation of ions from Earle's solution.

5. The anti-biofilm formation studies of the uncoated and anodized sample in gram-negative

(*P. aeruginosa*) and gram-positive (*S. epidermis*) bacteria showed biofilm inhibition reduced rate of 15% and 20% of biofilm formation.

Hence, it was concluded that silicate coating was satisfying the basic criteria for its usage in orthopedic implant.

References

[1] Catt K, Li H, Cui XT (2017) Poly (3, 4-ethylenedioxythiophene) graphene oxide composite coatings for controlling magnesium implant corrosion. Acta Biomater 48:530–540

[2] Ou C, Lu W, Zhan Z, Huang P, Yan P, Yan B, Minsheng C (2013) Effect of Ca and P ion concentrations on the structural and corrosion properties of biomimetic Ca-P coatings on ZK60 magnesium alloy. Int J Electrochem Sci 8:9518–9530

[3] Bakhsheshi-Rad H, Hadisi Z, Hamzah E, Ismail A, Aziz M, Kashefian M (2017) Drug delivery and cytocompatibility of ciprofloxacin loaded gelatin nanofibers-coated Mg alloy. Mater Lett 207:179–182

[4] Ding Y, Wen C, Hodgson P, Li Y (2014) Effects of alloying elements on the corrosion behavior and biocompatibility of biodegradable magnesium alloys: a review. J Mater Chem 2:1912–1933

[5] Sezer N, Evis Z, Kayhan SM, Tahmasebifar A, Koc M (2018) Review of magnesium-based biomaterials and their applications. J Magnes Alloys 6:23–43

[6] Jiang HB, Wu G, Lee SB, Kim KM (2017) Achieving controllable degradation of a biomedical magnesium alloy by anodizing in molten ammonium bifluoride. Surf Coat Technol 313:282–287

[7] Razavi M, Fathi M, Savabi O, Beni BH, Vashaee D, Tayebi L (2014) Surface microstructure and in vitro analysis of nanostructured akermanite ($Ca_2MgSi_2O_7$) coating on biodegradable magnesium alloy for biomedical applications. Colloids Surf B Biointerfaces 117:432–440

[8] Amaravathy P, Sathyanarayanan S, Sowndarya S, Rajendran N (2014) Bioactive HA/TiO_2 coating on magnesium alloy for biomedical applications. Ceram Int 40:6617–6630

[9] Mousa HM, Hussein KH, Woo HM, Park CH, Kim CS (2015) One-step anodization deposition of anticorrosive bioceramic compounds on AZ31B magnesium alloy for biomedical application. Ceram Int 41:10861–10870

[10] Xj Cui, Lin XZ, Liu CH, Yang RS, Zheng XW, Gong M (2015) Fabrication and corrosion resistance of a hydrophobic micro-arc oxidation coating on AZ31 Mg alloy. Corros Sci 90:402–412

[11] Reyes Y, Duran A, Castro Y (2016) Glass-like cerium sol-gel coatings on AZ31B magnesium alloy for controlling the biodegradation of temporary implants. Surf Coat Technol 307:574–582

[12] Wu L, Yang D, Zhang G, Zhang Z, Zhang S, Tang A, Fusheng P (2018) Fabrication and characterization of Mg-M layered double hydroxide films on anodized magnesium alloy AZ31. Appl Surf Sci 431:177–186

[13] Srinivasan A, Shin KS, Rajendran N (2016) Influence of bicarbonate concentration on the conversion layer formation onto AZ31 magnesium alloy and its electrochemical corrosion behaviour in simulated body fluid. RSC Adv 6:49910–49922

[14] Mousa HM, Hussein KH, Pant HR, Woo HM, Park CH, Kim CS (2016) In vitro degradation behavior and cytocompatibility of a bioceramic anodization films on the biodegradable magnesium alloy. Colloids Surf A Physicochem Eng Asp 488:82–92

[15] Xue D, Yun Y, Schulz MJ, Shanov V (2011) Corrosion protection of biodegradable magnesium implants using anodization. Mater Sci Eng C 31:215–223

[16] Mizutani Y, Kim S, Ichino R, Okido M (2003) Anodizing of Mg alloys in alkaline solutions. Surf Coat Technol 169:143–146

[17] Li W, Li W, Zhu L, Liu H, Wang X (2013) Non-sparking anodization process of AZ91D magnesium alloy under low AC voltage. Mater Sci Eng B 178:417–424

[18] Fatimah S, Kamil M, Kwon J, Kaseem M, Ko Y (2017) Dual incorporation of SiO$_2$ and ZrO$_2$ nanoparticles into the oxide layer on 6061 Al alloy via plasma electrolytic oxidation: coating structure and corrosion properties. J Alloys Compd 707:358–364

[19] Arunnellaiappan T, Arun S, Hariprasad S, Gowtham S, Ravisankar B, Rameshbabu N (2018) Fabrication of corrosion resistant hydrophobic ceramic nanocomposite coatings on PEO treated AA7075. Ceram Int 44:874–884

[20] Lu X, Feng X, Zuo Y, Zhang P, Zheng C (2017) Improvement of protection performance of Mg-rich epoxy coating on AZ91D magnesium alloy by DC anodic oxidation. Prog Org Coat 104:188–198

[21] El Mahallawy N, Shoeib M, Abouelenain M (2011) AZ91 magnesium alloys: anodizing of using environmental friendly electrolytes. J Surf Eng Mater Adv Technol 1:62–72

[22] Xiong Y, Yang Z, Hu X, Song R (2019) Bioceramic coating produced on AZ80 magnesium alloy by one-step microarc oxidation process. J Mater Eng Perform 28:1719–1727

[23] Xue Y, Pang X, Jiang B, Jahed H (2019) Corrosion and corrosion fatigue performances of micro-arc oxidation coating on AZ31B cast magnesium alloy. Mater Corros 70:268–280

[24] Giron L, Aperador W, Tirado L, Franco F, Caicedo J (2017) Electrochemical performance estimation of anodized AZ31B magnesium alloy as function of change in the current density. J Mater Eng Perform 26:3710–3718

[25] Dey A, Rani RU, Thota HK, Sharma AK, Bandyopadhyay P, Mukhopadhyay AK (2013) Microstructural, corrosion and nanomechanical behaviour of ceramic coatings developed on magnesium AZ31 alloy by micro arc oxidation. Ceram Int 39:3313–3320

[26] Jamali SS, Moulton SE, Tallman DE, Forsyth M, Weber J, Wallace GG (2014) Applications of scanning electrochemical microscopy (SECM) for local characterization of AZ31 surface during corrosion in a buffered media. Corros Sci 86:93–100

[27] Izquierdo J, Nagy L, Bitter I, Souto RM, Nagy G (2013) Potentiometric scanning electrochemical microscopy for the local characterization of the electrochemical behaviour of magnesium-based materials. Electrochim Acta 87:283–293

[28] Souto RM, Kiss A, Izquierdo J, Nagy L, Bitter I, Nagy G (2013) Spatially-resolved imaging of concentration distributions on corroding magnesium-based materials exposed to aqueous environments by SECM. Electrochem Commun 26:25–28

[29] Simoes A, Battocchi D, Tallman D, Bierwagen G (2007) SVET and SECM imaging of cathodic protection of aluminium by a Mg-rich coating. Corros Sci 49:3838–3849

[30] Simoes A, Battocchi D, Tallman D, Bierwagen G (2008) Assessment of the corrosion protection of aluminium substrates by a Mg-rich primer: EIS, SVET and SECM study. Prog Org Coat 63:260–266

[31] Bryant JC (1975) Earle's balanced salt solution: preparation of the saline. TCA Man/Tissue Cult Assoc 1:185–187

[32] Saranya K, Raja STK, Subhasree R, Gnanamani A, Das SK, Rajendran N (2017) Fabrication of nanoporous sodium niobate coating on 316L SS for orthopaedics. Ceram Int 43:11569–11579

[33] Stern M, Geary AL (1957) Electrochemical polarization I. A theoretical analysis of the shape of polarization curves. J Electrochem Soc 104:56–63

[34] Agilan P, Rajendran N (2018) In-vitro bioactivity and electrochemical behavior of polyaniline encapsulated titania nanotube arrays for biomedical applications. Appl Surf Sci 439:66–74

[35] Liu X, Zhang T, Shao Y, Meng G, Wang F (2009) Effect of alternating voltage treatment on the corrosion resistance of pure magnesium. Corros Sci 51:1772–1779

[36] Jun D, Liang J, Hu LT, Hao JC, Xue QJ (2007) Effects of sodium tungstate on characteristics of microarc oxidation coatings formed on magnesium alloy in silicate-KOH electrolyte. Nonferrous Met Soc China 17:244–249

[37] Duan H, Yan C, Wang F (2007) Growth process of plasma electrolytic oxidation films formed on magnesium alloy AZ91D in silicate solution. Electrochim Acta 52:5002–5009

[38] Chai L, Yu X, Yang Z, Wang Y, Okido M (2008) Anodizing of magnesium alloy AZ31 in alkaline solutions with silicate under continuous sparking. Corros Sci 50:3274–3279

[39] Amaravathy P, Rose C, Sathiyanarayanan S, Rajendran N (2012) Evaluation of in vitro bioactivity and MG63 oesteoblast cell response for TiO_2 coated magnesium alloys. J Sol-Gel Sci Technol 64:694–703

[40] Kuo YL, Chang KH (2015) Atmospheric pressure plasma enhanced chemical vapor deposition of SiOx films for improved corrosion resistant properties of AZ31 magnesium alloys. Surf Coat Technol 283:194–200

[41] Saranya K, Kalaiyarasan M, Suvrao C, Rajendran N (2019) Dynamic electrochemical impedance study of fluoride conversion coating on AZ31 magnesium alloy to improve bioadaptability for orthopedic application. Mater Corros 70(4):698–710

[42] Leventouri T, Bunaciu C, Perdikatsis V (2003) Neutron powder diffraction studies of silicon-substituted hydroxyapatite. Biomaterials 24:4205–4211

[43] Xu Q, Liu Y, Liu C, Tian A, Shi X, Dong C, Zhoua X, Zhoua H (2015) Performance of hydroxyapatite coatings electrodeposited on micro-arc oxidized magnesium alloys using a static magnetic field. RSC Adv 5:14458–14464

[44] Aktug SL, Durdu S, Kutbay I, Usta M (2016) Effect of $Na_2SiO_3 \cdot 5H_2O$ concentration on microstructure and mechanical properties of plasma electrolytic oxide coatings on AZ31 Mg alloy produced by twin roll casting. Ceram Int 42:1246–1253

[45] Salami B, Afshar A, Mazaheri A (2014) The effect of sodium silicate concentration on microstructure and corrosion properties of MAO-coated magnesium alloy AZ31 in simulated body fluid. J Magn Alloys 2:72–77

[46] Gao H, Zhang M, Yang X, Huang P, Xu K (2014) Effect of Na_2SiO_3 solution concentration of micro-arc oxidation process on lap-shear strength of adhesive-bonded magnesium alloys. Appl Surf Sci 314:447–452

[47] Durdu S, Bayramoglu S, Demirtas A, Usta M, Ucisikk AH (2013) Characterization of AZ31 Mg Alloy coated by plasma electrolytic oxidation. Vacuum 88:130–133

[48] Simi V, Satish A, Korrapati PS, Rajendran N (2018) In-vitro biocompatibility and corrosion resistance of electrochemically assembled PPy/TNTA hybrid material for biomedical applications. Appl Surf Sci 445:320–334

[49] Amaravathy P, Sowndarya S, Sathyanarayanan S, Rajendran N (2014) Novel sol gel coating of Nb_2O_5 on magnesium alloy for biomedical applications. Surf Coat Technol 244:131–141

[50] Alabbasi A, Kannan MB, Walter R, Stormer M, Blawert C (2013) Performance of pulsed constant current silicate-based PEO coating on pure magnesium in simulated body fluid. Mater Lett 106:18–21

[51] Liu H, Sha W, Cooper AT, Fan M (2009) Preparation and characterization of a novel silica aerogel as adsorbent for toxic organic compounds. Colloids Surf A Physicochem Eng Asp 347:38–44

[52] Spriano S, Bosetti M, Bronzoni M, Verne E, Maina G, Bergo V (2005) Surface properties and cell response of low metal ion release Ti-6Al-7Nb alloy after multi-step chemical and thermal treatments. Biomaterials 26:1219–1229

[53] Huo W, Lin X, Yu S, Yu Z, Zhang W, Zhang Y (2019) Corrosion behavior and cytocompatibility of nano-grained AZ31 Mg alloy. J Mater Sci 54:4409–4422. https://doi.org/10.1007/s10853-018-3149-8

[54] Srinivasan A, Ranjani P, Rajendran N (2013) Electrochemical polymerization of pyrrole over AZ31 Mg alloy for biomedical applications. Electrochim Acta 88:310–321

[55] Jamesh M, Kumar S, Narayanan TS (2011) Corrosion behavior of commercially pure Mg and ZM21 Mg alloy in Ringer's solution–Long term evaluation by EIS. Corros Sci 53:645–654

[56] Zhang Q, Ye Z, Zhu Z, Liu X, Zhang J, Cao F (2018) Separation and kinetic study of iron corrosion in acidic solution via a modified tip generation/substrate collection mode by SECM. Corr. Sci 139:403–409

[57] Zhang Y, Liu X, Jamali SS, Hinton BR, Moulton SE, Wallace GG, Maria F (2016) The effect of treatment time on the ionic liquid surface film formation: promising surface coating for Mg alloy AZ31. Surf Coat Technol 296:192–202

[58] Salman S, Kuroda K, Okido M (2013) Preparation and characterization of hydroxyapatite coating on AZ31 Mg alloy for implant applications. Bioinorg Chem Appl. https://doi.org/10.1155/2013/175756

[59] Ma H, Gu Y, Liu S, Che J, Yang D (2017) Local corrosion behavior and model of micro-arc oxidation HA coating on AZ31 magnesium alloy. Surf Coat Technol 331:179–188

[60] Capeletti LB, de Oliveira LF, Goncalves KA, Oliveira JFA, Saito AN, Kobarg JR, Mateus Borba C (2014) Tailored silica–antibiotic nanoparticles: overcoming bacterial resistance with low cytotoxicity. Langmuir 30:7456–7464